Future Batteries 7 (2025) 100095

Contents lists available at ScienceDirect

Future Batteries

journal homepage: www.sciencedirect.com/journal/future-batteries

Towards anode-less lithium metal negative electrodes for secondary aprotic batteries

Antonio Santagata [a], Maria Lucia Pace [a], Daniele Maria Trucchi [a], Mariangela Curcio [b], Angela De Bonis [b], Roberto Teghil [b], Nicholas Carboni [c], Andrea Gentile [c], Arianna Sette [c], Luca Mesina [c], Andrea Ceppetelli [c], Laura Silvestri [e], Paola Gislon [e], Giuseppe Antonio Elia [f], Marisa Falco [f], Gabriele Lingua [f], Claudio Gerbaldi [f], Maria Assunta Navarra [c], Marco Agostini [d], Sergio Brutti [c,*]

[a] CNR-ISM, U.O.S. Tito Scalo, Zona Industriale, Tito Scalo 85050, Italy
[b] Dipartimento di Scienze di Base e Applicate, Università della Basilicata, V.le dell'Ateneo Lucano 10, Potenza 85100, Italy
[c] Dipartimento di Chimica, Università di Roma La Sapienza, P.le Aldo Moro 5, Roma 00185, Italy
[d] Dipartimento di Chimica e Tecnologie del Farmaco, Università di Roma La Sapienza, P.le Aldo Moro 5, Roma 00185, Italy
[e] ENEA C.R. Casaccia, Roma 00123, Italy
[f] GAME Lab, Department of Applied Science and Technology (DISAT), Politecnico di Torino, Corso Duca degli Abruzzi 24, Torino 10129, Italy

ARTICLE INFO

Keywords:
Lithium metal
Anode-less electrodes
Aprotic batteries
Secondary batteries
Metal batteries
Laser induced periodic surface structures
Artificial solid electrolyte interphase

ABSTRACT

This study presents the synergistic application of optimized laser-induced periodic surface structure (LIPSS) patterning conducted under ambient conditions and the deposition of an artificial solid-state electrolyte (aSEI) for the fabrication of a novel lithium-less lithium metal electrode (L^3ME) utilizing stainless steel (SS). The composite anode-less substrate demonstrates the capability to facilitate the reversible plating and stripping of metallic lithium over several hundred cycles in aprotic battery systems. The LIPSS technique generates a patterned surface characterized by micrometer-long ripples with a lateral periodicity ranging from 150 to 250 nm, whereas the deposition of the aSEI results in a uniform and smooth surface morphology achieved through the homogeneous dispersion of a polymeric-inorganic composite film. This research unveils, for the first time in the literature, the synergistic combination of laser patterning and aSEI pre-deposition, thereby advancing current methodologies for anode-less electrode fabrication. An extensive analysis was conducted on varying LIPSS patterning conditions and aSEI compositions to assess their implications on electrochemical performance. The constructed L^3ME comprises a stainless steel thin foil featuring a mesostructured surface marked by a regular distribution of iron (Fe) and iron oxide (Fe_2O_3) ripples. This structured surface is seamlessly integrated beneath a uniform polyethylene oxide and lithium nitrate composite film, allowing for the manufacture, handling, and storage of L^3ME substrates in dry air, eliminating the necessity for inert atmosphere conditions. The optimized L^3ME electrodes exhibit remarkable performance in aprotic lithium cells, facilitating fully reversible metallic lithium stripping and deposition, with exceptionally high coulombic efficiencies nearing 100 % over numerous cycles across various galvanostatic conditions that adhere to commercial standards (current densities of 0.25–1.25 mA cm^{-2} and areal capacity limits from 0.5 to 5 mAh cm^{-2}). Comparative benchmarking of L^3ME performance against bare copper electrodes and other anode-less substrates highlights the distinctive efficacy of the combined LIPSS and aSEI technique in enhancing the reversibility of lithium plating and stripping through a selective inhibition of electrochemical lithium dissolution.

Introduction

Green and sustainable energy storage technologies are currently in the spotlight of public interest[1–4]. Over the last three decades, significant investments in research and development from companies, academia, and national laboratories have facilitated the evolution of

* Corresponding author.
E-mail address: Sergio.brutti@uniroma1.it (S. Brutti).

https://doi.org/10.1016/j.fub.2025.100095
Received 22 May 2025; Received in revised form 30 June 2025; Accepted 17 July 2025
Available online 19 July 2025

batteries capable of powering the transition from mobile devices to portable electronics, power tools, and hybrid electric vehicles[5–11]. This remarkable technological shift is rooted in the chemistry of lithium-ion intercalation and its unique versatility[12–18]. The puzzle of optimizing active materials at electrodes alongside tailored electrolyte formulations (i.e., liquid, gel, polymeric, or solid) allows for fine tuning the performance of lithium-ion batteries (LIBs) to meet the requirements of various specific applications[2,4,6,8,16,19]. Unfortunately, the lithium-ion intercalation paradigm is approaching its theoretical limits, thereby opening the search for novel flexible processes to store energy in batteries for upcoming technological challenges, which include large-scale stationary energy storage from renewable sources and full electric mobility[20–23]. Various solutions have been proposed, studied, and demonstrated, ranging from alloying [24] and conversion[25–27] to anionic redox couples[28–31] and multivalent cations [32–34], with the ultimate goal being a breakthrough in enhancing electrode performance without compromising safety, sustainability, and costs [1,16,23,35,36].

Among the proposed methods, the electrochemical plating and stripping of lithium metal at the negative electrode can potentially result in a significant performance leap, owing to the exceptional theoretical capacitative figures of lithium metal electrodes (Q_{th} = 3860 mAhg^{-1} and E° = –3.04 V vs SHE, standard hydrogen electrode), as compared to commercial negative graphite electrodes for LIBs (Q_{th} =372 mAhg^{-1} and ≈ – 2.9 V vs SHE), or the state-of-the-art research-grade negative silicon conversion electrodes Q_{th} = 3579 mAhg^{-1} and ≈ – 2.8 V vs SHE) [37–44]. However, lithium metal electrodes experience poor coulombic efficiency (CE) upon cycling in batteries due to their propensity to form heterogeneous and non-uniform surface morphologies at the nano- and meso-scales, such as dendrites and dead lithium[43,44]. A wide variety of strategies have been proposed to address this unavoidable problem, which stems from the thermodynamic instability of any metallic lithium/aprotic electrolyte active interface. Almost all aprotic polar electrolytes capable of facilitating lithium ion transport operate outside their thermodynamic stability window at the negative electrodes in LIBs, particularly on lithium metal[45–49]. Generally, advances in the electrochemical reversibility of lithium stripping and deposition have been achieved through various methodologies, including:

- Tuning the electrolyte formulation to promote the formation of a passivation film on lithium or to modulate the electrocrystallization/dissolution [37,50–53].
- Preforming suitable solid electrolyte interphases on lithium that can mitigate parasitic reactivity during cycling and buffer volume changes[40,50,54–58].
- Alloying lithium with aluminum (or indium, zinc, bismuth, or arsenic) to enhance the nucleation and growth of smooth and homogeneous lithium deposits[59–65].
- Developing and optimizing three-dimensional open morphologies for copper current collectors to accommodate the nucleation and growth of lithium[66–68].

Here we investigate the use of AISI 316 stainless-steel (SS) foil electrodes structured with femtosecond laser-induced periodic surface structures (LIPSS) coated with a hybrid artificial solid electrolyte interphase (aSEI) as anode-less (or lithium-less) lithium metal electrodes (L^{3}MEs). We successfully tested L^{3}MEs in lab-scale lithium metal aprotic batteries containing a 1 M $LiPF_6$ liquid solution in a mixture of ethylene carbonate and dimethyl carbonate (EC:DMC, 1:1 by volume) electrolyte. Our approach leverages the synergistic formation of extensive regular meso-ripples on the SS surface combined with the deposition of a uniform coating made from poly-ethylene oxide (PEO) polymeric film. This combination promotes facile electrochemical nucleation of lithium, buffers volume changes during cycling in batteries, and effectively mitigates dendrite formation thanks to fine-tuning of the electrokinetics. Through this strategy, the authors demonstrate a fully reversible deposition and stripping of lithium metal on L^{3}MEs (Q_{rev} = 0.25 mAhcm^{-2}) at 0.25 mAcm^{-2} o ver hundreds of cycles without capacity loss, thereby achieving nearly 100 % CE at room temperature in a standard liquid electrolyte.

The primary distinction between the L^{3}ME electrodes and state-of-the-art anodeless negative electrodes for lithium metal batteries lies in the synergistic combination of laser patterning and pre-deposition of an aSEI going beyond the standard approaches summarized above. As a consequence the L^{3}ME electrodes demonstrate a significantly larger exchange current density (J_0), which is approximately three times higher than that of traditional copper electrodes. This enhancement suggests a more efficient lithium electrochemical reduction and oxidation process, marking a substantial advancement over existing technologies. Moreover, the LIPSS technique boasts a minimal environmental impact and scalability, making it a more sustainable option compared to traditional fabrication methods. Thus, the integration of L^{3}ME electrodes not only improves performance but also contributes to the development of environmentally conscious energy storage solutions.

Materials and methods

Materials and preparation routes

AISI 316 stainless steel (SS, MTI Corp), copper (Cu, MTI Corp) as well as carbon-coated copper (C@Cu, MTI Corp) foils have been used in disks of 10 mm in diameters. The preparation of the L^{3}MEs samples implies two subsequent steps of surface modification starting from a SS foil: (a) LIPSS pattering (LIPSS@SS sample) and (b) aSEI coating (SS@E and L^{3}ME samples).

LIPSS pattering has been obtained by a, Spectra Physics Spitfire Amplifier linearly polarized Ti:Sapphire femtosecond laser (τ = 120 fs; λ = 800 nm, ν = 1 kHz) focused on the SS foil. The SS foil has been positioned onto a motorized sample translation stage to induce a homogeneous patterning of round areas with controlled dimensions (LIPSS@SS). A variety of LIPSS patterning conditions can be finely tunes to obtain specific nano-morphologies drawn over the target surface. The conditions identified for the LIPSS@SS manufacture are: scanning speed and interline distance of 1500 μm/s and 20 μm, respectively, accumulation of 86 effective laser pulses, fluence 0.5 J/cm^2 The LIPSS has been induced in air and successively sonicated in ethanol for 15 min for removing superficial deposited debris and, afterwards, the pattered areas have been cut in round disks that, after vacuum drying at 120 °C, have been transferred into the glove box.

The deposition of an aSEI film is realized into the glove box by drop casting on the round LIPSS@SS samples a precursor solution constituted by polyethylene oxide (PEO, Solvay) with mean molecular weight 150 kD and $LiNO_3$ (Sigma Aldrich) dissolved in acetonitrile (Sigma Aldrich). This last solvent is gently evaporated at room temperature in the glove box (Iteco Eng SGS30, ppm_{H2O}<0.1) followed by mild vacuum to preserve the morphological integrity of the film and avoid any moisture contamination. Other aSEI compositions have been preliminary screened (see the SI, application note 2 for mor details) by using acetonitrile (Sigma Aldrich), tetrahydrofuran (Sigma Aldrich), polyethylene oxide with different mean molecular weight in Dalton (MTI Corp. and Solvay), carboxymethyl cellulose (MTI Corp), polyvinyl difluoride (MTI Corp), lithium bis(trifluoromethyl sulphonyl) imide (Solvionic), lithium hexafluorophosphate (Sigma Aldrich) and $Li_{6.4}La_3Zr_{1.4}Ta_{0.6}O_{12}$ (MTI Corp).

Cell assembly, electrochemical tests and post mortem sample preparation

SS, SS@E, LIPSS@SS, Cu, C@Cu and L^{3}ME samples have been tested as positive electrodes in lithium metal cells using Celgard (El Cell) or Whatman separators, a 1 M solution of lithium hexafluorophosphate dissolved in a 1:1 vol mixture of ethylene carbonate (EC) dimethyl

carbonate (DMC) electrolyte (Solvionic) and a lithium metal counter electrode (Chemetall Gmbh). El-Cell Std cells have been used for the electrochemical tests to allow a facile cell de-assembly to collect post-mortem samples. Capacities and currents have been all normalized by the geometrical electrode surfaces (0.785 cm^2). Galvanostatic cycling have been performed using a MTI battery test apparatus: cells have been kept at constant temperature (30°C) using a static oven (Memmert). Coulombic efficiencies (CE) have been calculated as the ratio between the discharge (plating) and the charge (stripping) capacities at a given cycle number. Chronopotentiometric tests have been performed by using an Ivium Vertex potentiostat/galvanostat/EIS apparatus as well as impedance spectroscopy tests (EIS, 10 kHz,-0.1 Hz, ΔV=10 mV). Samples have been collected post mortem for further characterization by de-assembling the electrochemical cells. Post mortem materials have been washed in DMC and THF to remove traces of the lithium salts, solvents have been removed by gentle dynamic vacuum at room temperature: the final dry samples have been stored in an Ar-filled glove box before further characterization.

Electro-kinetics parameters analysis by the Butler-Volmer equation for monoelectronic reactions. Electro-kinetic parameters have been evaluated using the well-known Butler Volmer equation:

$$J = J_o \bullet \left\{ e^{\frac{\beta F\eta}{RT}} - e^{-\frac{(1-\beta)F\eta}{RT}} \right\} \quad (1)$$

where J is the experimental current density (mA cm^{-2}), J_0 is the exchange current density (mA cm^{-2}), β is the anodic charge transfer coefficient, F is the Faraday constant, R is the Gas constant, T is the temperature and η is the kinetic overvoltage. Galvanostatic plating/stripping pre-conditioning cycles (five) at 0.25 $mAcm^{-2}$ (cutoff areal discharge 0.25 $mAhcm^{-2}$) have been carried out to stabilize the electrode surfaces. Galvanostatic tests have been performed at various current densities during plating/stripping to record the experimental overpotentials for each electrode material. Experimental overpotentials versus current densities datasets have been analyzed by a home-made non-linear fitting algorithm (available at the corresponding author).

Materials characterization techniques

XPS spectra have been recorded by a Phoibos 100-MCD5 (SPECS GmBH, Berlin, Germany) spectrometer, using non-monochromatized AlK radiation (1486.6 eV) operating at 10 kV and 10 mA. Wide and detailed spectra were collected in Fixed Analyzer Transmission (FAT) mode with a pass energy of 50 eV and channel widths of 1.0 and 0.1 eV, respectively. XPS samples have been transferred into the spectrometer through an argon-filled glove-bag directly connected to the fast entry lock chamber of the instrument without contact with air, to avoid possible moisture/CO2 contaminations. The experimental spectra have been theoretically reconstructed by the means of "Googly" program[69], that allows to fit each peak with a Voigt function taking into account both intrinsic and extrinsic contribution and the associated background. The Gaussian-to-Lorentzian ratio varied between 0.7 and 0.9. XPS atomic ratios between relevant core lines have been estimated from experimentally determined area ratios corrected for the corresponding Scofield cross sections [28] and for a square root dependence of the photoelectrons kinetic energies. No sign of sample degradation upon extended acquisition times under the X-rays has been observed. Scanning electron micrographs have been recorded by using a field emission scanning electron microscope (FESEM) at the CNIS research centre (ZEISS Auriga) equipped with an energy dispersive X-ray probe (EDX) for the elemental analysis of samples. SEM micrographs have been analyzed by the ImageJ software[70]. FTIR spectra have been obtained by an ATR (germanium crystal) FTIR Bruker alpha apparatus: samples have been analyzed in an Ar-filled glove box to preserve their integrity and avoid hydrolysis.

Results and discussion

The preparation of the L^3ME samples involves two successive steps of surface modification, beginning with a stainless steel (SS) foil, as shown schematically in Fig. 1.

The LIPSS patterning, i.e. the formation of periodic surface structures, is induced by a linearly polarized Ti:Sapphire femtosecond laser (pulse length $\tau = 120$ fs; wavelength $\lambda = 800$ nm, repetition rate $\nu = 1$ kHz) focused on the stainless-steel (SS) foil by a 4X magnifying optics and numeric aperture of 0.10. The SS foil is positioned on a motorized sample translation stage to induce homogeneous patterning of round disks with controlled dimensions (LIPSS@SS). A variety of LIPSS patterning conditions can be finely tuned to obtain specific nano-morphologies inscribed on the target surface[71]. A survey of the impact of laser irradiation conditions on the final meso-structure is presented in the supplementary information (SI) application note 1. The conditions identified for the manufacture of the electrode materials are the scanning speed and an interline distance of 1550 μm s^{-1} and 30 μm, respectively, with a laser pulse duration of 180 fs and a laser power of 135 mW. The LIPSS is induced in air and afterwards the pattered areas are cut in round disks that, after washing in ethanol and vacuum drying at 120 °C, are transferred into the glove box. The LIPSS procedure has a very limited environmental footprint, as it does not involve the use of solvents or other chemicals. It is easily scalable to large areas and is characterized by very high definition, which is also useful for developing optical meta-surfaces [72–74].

The deposition of an aSEI film is performed within a glove box by drop casting from a precursor solution (a-SEI9@Li; see the SI application note 2) onto the round LIPSS@SS samples. This precursor solution consists of polyethylene oxide (PEO) with a mean molecular weight of 150 kD and $LiNO_3$ dissolved in acetonitrile. The acetonitrile solvent is gently evaporated at room temperature in the glove box, followed by mild vacuum treatment to preserve the morphological integrity of the film and prevent any moisture contamination. To improve the sustainability of this procedure, the use of acetonitrile is minimized, ultimately utilizing less than 100 microliters per square centimeter of L^3ME. The composition of the aSEI has been preliminarily optimized by screening the performance of various aSEIs in Li/Li symmetric cells. A summary of this analysis is presented in the supplementary information (SI), application note 2.

LIPSS is an established technique that promotes controlled ablation and patterning of materials, including both metals and semiconductors, by exploiting focused pulsed laser irradiation [71–74]. If the used laser pulses have ultrashort duration in the femtosecond range, all the thermal effects are minimized as well as post-melting and undesired fracture propagations outside the treated material zone. Consequently, the resulting LIPSS has a far higher resolution and reproducibility than the case of using longer pulse lasers. The alterations of the surface morphology induced by LIPSS on the SS samples (i.e. LIPSS@SS) and the following changes induced by the aSEI coating (i.e. L^3ME) are highlighted in the scanning electron micrographs (SEM) shown in the Fig. 1b-c-d. As expected, the laser treatment strongly alters the smooth surface of the SS pristine foil, forming elongated micrometer-long ripples with lateral size in the 150–250 nm range.

The coating with the aSEI reinstates a smooth surface over the ripples, thanks to the homogeneous distribution of the film constituents, as highlighted in the energy-dispersive X-ray spectroscopy (EDX) analysis. Atomic distribution maps for carbon, oxygen, and nitrogen are presented in the supplementary information (Figure S7, SI).

The analysis of the surface composition by x-ray photoemission (XP) spectroscopy confirms that the aSEI deposited on the L^3ME sample homogeneously fills the ripples and covers the underlying SS surface, being missing the Fe 2p signal (see the Fig. 2a, on passing we note that, as expected, the presence of the N 1S signal is observed only on the L^3ME sample, for more technical details kindly refer to below the experimental section).

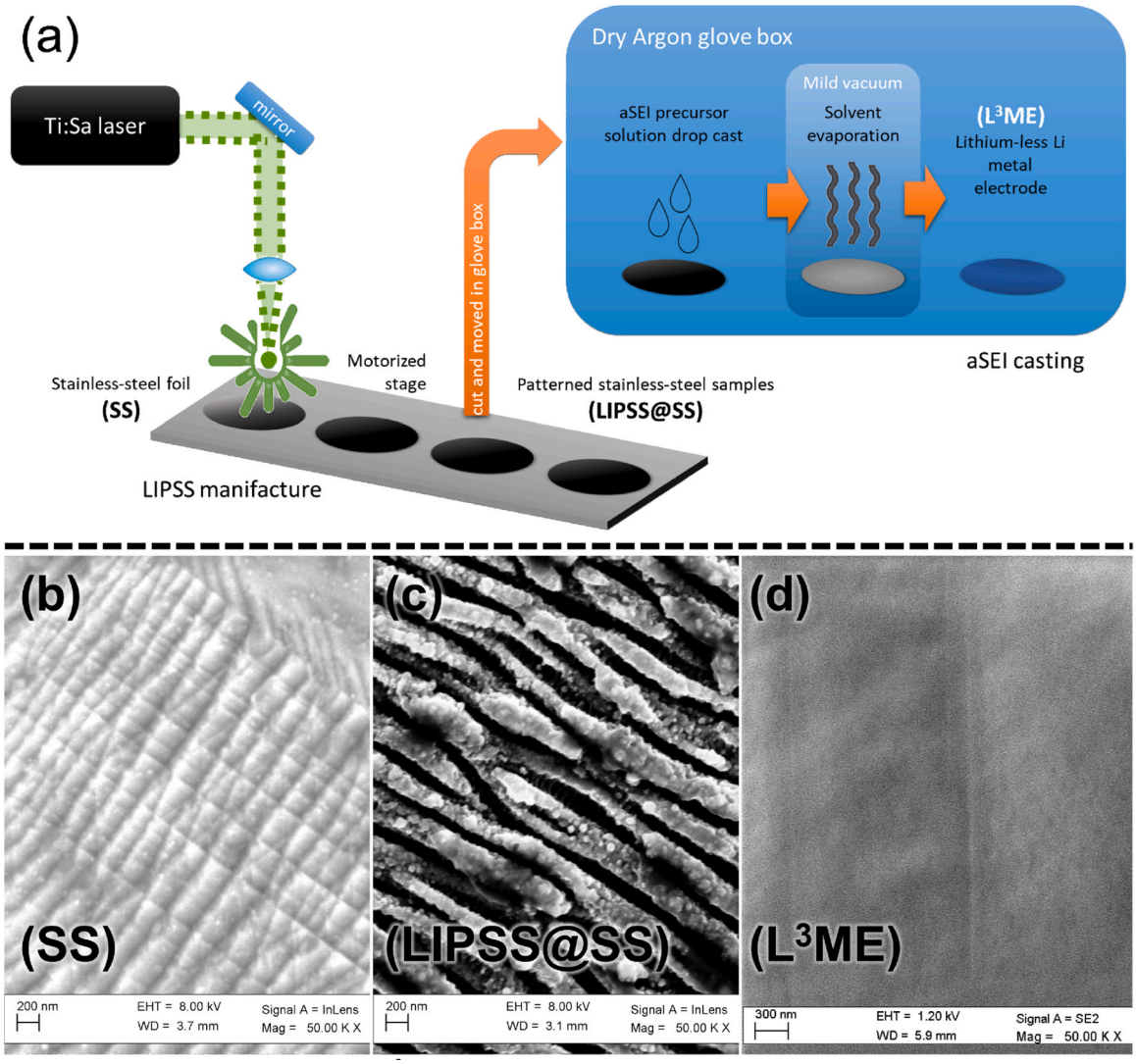

Fig. 1. Visual cartoon of the L^3MEs sample preparation including (a) the LIPSS processing of the stainless-steel foil and the subsequent aSEI formation by drop casting in the glove box. (b-c-d) Scanning electron micrographs of the SS, LIPSS@SS and L^3ME samples at the same magnification (50k x).

The XP spectral theoretical reconstructions of the C 1 s, O 1 s, N 1 s and Li 1 s regions confirm that the aSEI on the L^3ME surface is constituted by PEO, $LiNO_3$ and traces of nitrites and CH_3CN (Fig. 2b-c-d and figure S8 in the SI). Similar theoretical reconstructions of the XP spectra performed on the C 1 s, O 1 s and Fe 2p regions of the uncoated SS and LIPSS@SS samples suggest that the LIPSS process partially oxidize the SS surface (see table S3, SI), leading to the accumulation of Fe_2O_3 and oxidized carbon species over metallic iron.

To shed more light on the morphological properties of the anodeless electrodes holes have been manufactured on the LIPSS and L^3ME substrates by a focused ion beam (FIB) in the SEM apparatus to partially dig into the ripples and remove the aSEI, respectively. SEM micrographs of the tiled surfaces of the LIPSS and L^3ME substrates are shown in the Fig. 2e-f: apparently the ripples on the LIPSS substrate shown heights of approximately 200–400 nm whereas the aSEI is 4–6 micrometers thick.

Overall, the L^3ME materials are stainless steel (SS) thin foils with a mesostructured surface patterned by a regular distribution of ripples composed of Fe and Fe2O3. This regular surface pattern is situated beneath a uniform and smooth PEO-$LiNO_3$ composite film.

Once assembled in lithium metal half cells the L^3ME samples can reversibly exchange 0.25 mAh cm^{-2} areal capacity at a current density of $J = 0.25$ $mAcm^{-2}$ for hundreds of cycles (see Fig. 3a-b-c-d) at room temperature, outperforming bare copper electrodes in terms of plating/stripping reversibility with comparable overpotentials.

In fact, excluding the first lithium plating/stripping cycle where an overpotentials of 0.1 V is observed together with a coulombic efficiency below 50 %, L^3ME can reversibly accommodate lithium deposition and stripping with small overpotentials in line with the copper disks (charge overpotentials on L^3ME: 40–60 mV at cycle 1, 55–65 mV at cycle 10, 60–70 mV at cycle 100).

Generally speaking, bare lithium-less, or anode-less, metal electrodes are unable to assist reversible electrochemical lithium plating/stripping cycles in liquid electrolytes[75]. We confirmed experimentally the unsatisfactory performance of other lithium-less materials (i.e. Cu, SS or carbon coated copper, Cu@C) adopting the same galvanostatic condition successfully demonstrated for the L^3ME sample. The comparison of the CEs measured at room temperature using the same liquid electrolyte and adopting a current density of 0.25 $mAcm^{-2}$ and a limiting areal capacity of 0.25 $mAhcm^{-2}$ are shown in the Fig. 3d for L^3ME vs. Cu, and in the figure S9 (SI) for SS and Cu@C electrodes. With the exception of the L^3ME electrodes, the CEs of all metal electrodes are far from 100 % and are very scattered: this performance wastes charge and leads to the accumulation of dead lithium over the surface of the anode-less metal electrodes. The decoupling of the impact of LIPSS patterning and aSEI on the performance is discussed in the last section of this manuscript.

The poor and scattered reversibility of lithium plating and stripping

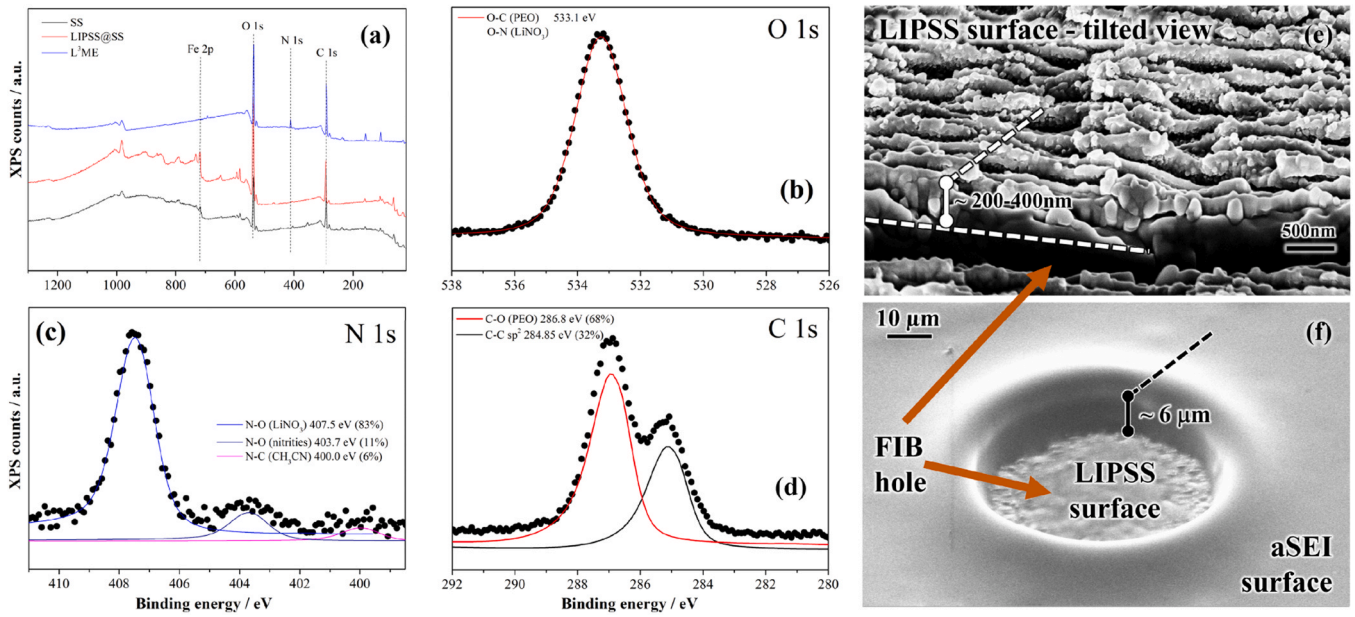

Fig. 2. (a) XP spectra of the SS, LIPSS@SS and L^{3}ME samples showing the deposition uniformity and composition of the aSEI, (b-c-d) detailed XP spectra and theoretical reconstructions for the O, N and C 1 s regions on the L^{3}ME electrodes; (e) SEM micrography of the tilted view of the LIPSS SS substrate; a micro-hole has been manufactured onto the LIPSS surface by using a focus ion beam (FIB) to allow an estimate of the ripples heights (i.e. 200–400 nm); (f) SEM micrography of the tilted view of the L^{3}ME electrode; a micro-hole has been manufactured to remove partially the aSEI by FIB, in order to evaluate of the aSEI thickness (i.e. 5–7 µm);.

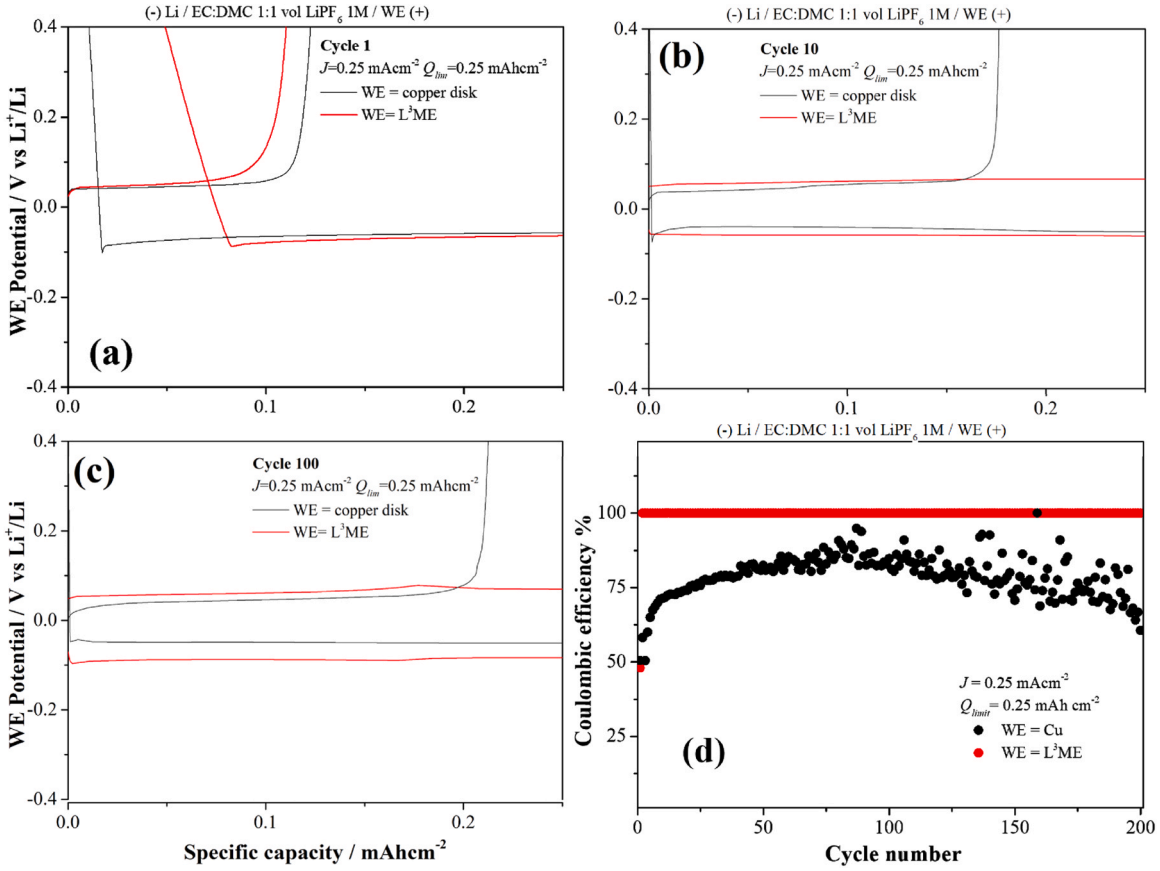

Fig. 3. Comparison of the working electrode (WE) potential profiles in discharge (lithium plating)-charge (lithium stripping) cycles at room temperature with a liquid electrolyte (EC.DMC 1:1 in volume, 1 M $LiPF_6$) using a $J = 0.25$ mAcm^{-2} and a limiting areal capacity of 0.25 mAhcm^{-2} and a Celgard separator. Charge-discharge cutoffs are set fixing a limiting areal capacity of 0.25 mAhcm^{-2} per step. (a) cycle 1; (b) cycle 10; (c) cycle 150; (d) Comparison of the measured coulombic efficiencies for Cu and L^{3}ME electrodes in lithium cells.

is not surprising on anode-less substrates using additive-free, unoptimized liquid electrolytes, as inhomogeneous lithium nucleation, growth, and dissolution lead to the formation of dendrites and dead lithium [75–77]. The inevitable consequence is the poor CE, largely below unity. In this respect the ability of L^3ME to support the reversibly plating/stripping of lithium at room temperature using a liquid electrolyte is outstanding.

It is important to underline that the charge potential changes observed or the optimized L^3ME electrodes after 100 cycles can be attributed to several interrelated factors. First, the formation and stability of the aSEI play a critical role in modulating electrochemical performance. As cycling progresses, the aSEI likely evolves, leading to modifications in its ionic conductivity and stability, which in turn affects lithium ion dynamics at the electrode surface. One may speculate that this dynamic evolution can result in a gradual increase in charge potential due to rising interfacial resistances and non-ideal lithium plating and stripping behavior. Another contributing factor to the potential changes is the electrochemical reaction kinetics associated with lithium metal at the electrode interface. The initial cycles benefit from low internal resistance due to favorable electrocrystallization pathways, but as cycling continues, reaction dynamics can shift, leading to higher overpotentials and, consequently, noticeable charge potential increases after 100 cycles.

In order to extend the performance validation of the L^3ME electrode concept, additional galvanostatic tests in lithium cells have been performed at room temperature at various current densities (i.e. 0.25–1.25 mA cm^{-2} at constant areal capacity of 0.25 mAh cm^{-2}) and at various areal capacity limits (0.5–5 mAh cm^{-2} at constant current density of 0.25 mA cm^{-2}). Results are shown in the SI in the figure S10 and confirm the outstanding ability of the L3ME electrodes to sustain reversible plating/stripping cycles under a variety of galvanostatic conditions.

The extraordinary electrochemical performance of the L^3ME electrodes reflects on the remarkable resilience of the surface LIPSS mesostructure upon cycling. In the Fig. 4 we compare the surface morphology by SEM of the L^3ME and Cu samples collected *post mortem* from batteries after lithium deposition (Q_{lim} = 0.25 mAhcm^{-2} at J = 0.25 mAcm^{-2}) and after 200 repeated cycles of plating/stripping (Q_{lim} = 0.25 mAhcm^{-2}, J = 0.25 mAcm^{-2}.

Lithium deposits nucleate on L^3ME and grow following the ripples morphology underneath the aSEI. A similar ripples-like morphology is also observed after 200 cycles of repeated stripping/deposition: apparently elongated meso-structures reminiscent of the original ripples can be observed throughout the entire surface, whereas small dendrites are almost absent. This is additional evidence of the strong impact of the surface patterning on the lithium nucleation/growth/dissolution electro-kinetics. Conversely the naturally rough Cu surfaces promote the growth of dendrites[7], easily observed after lithium deposition in Fig. 4e, and the accumulation of dead-lithium and byproducts upon cycling (see Fig. 4f).

We need to underline that the evidence of residual LIPSS mesomorphologies over the L^3ME electrodes collected after cycling likely suggests the strong alteration/removal of the SEI. This evidence originates from two competitive effects that cannot be easily decoupled: (a) the unavoidable swelling of PEO during the *postmortem* washing procedure and (b) the consolidation of the SEI layer promoted by the reactive interplay between aSEI components and the byproducts of the electrochemical degradation of the liquid electrolyte. Experimentally it

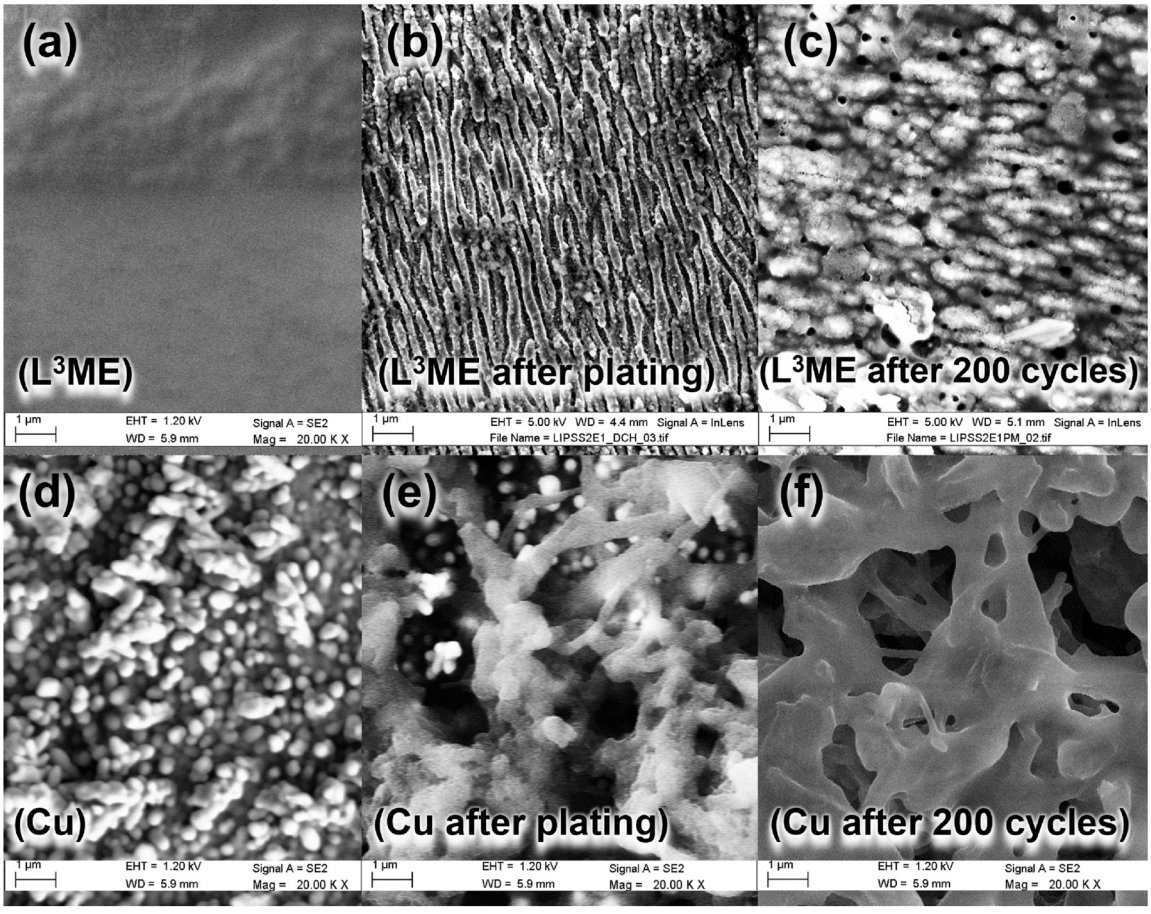

Fig. 4. Scanning electron micrographs of the L^3ME and Cu electrodes: (a,d) pristine; (b,e) collected *post mortem* from a lithium cell after plating (Q_{lim} = 0.25 mAhcm^{-2} at J = 0.25 mAcm^{-2}); (c,f) collected *post mortem* from a lithium cell after 200 cycles of plating/stripping (Q_{lim} = 0.25 mAhcm^{-2}, J = 0.25 mAcm^{-2}).

is possible to demonstrate that the impedance of the electrolyte/electrode interface at the L^{3}ME undergoes to relevant alterations during the first plating/stripping cycle, as demonstrated by impedance spectroscopy (EIS) in the SI (see figure S11 where the comparison of the evolution of the impedance spectra upon lithium plating/stripping on Cu and L^{3}ME is shown). In fact, the impedance of the inner layer on the L^{3}ME electrode change and stabilize upon plating/stripping likely inducing a consolidation of the SEI film[78]. This evidence closely matches the experimental evidence obtained by ex situ FTIR (Fig. 5) on the L^{3}ME electrodes, despite the unavoidably possible artifacts introduced by the postmortem washing procedure. A more detailed discussion of the EIS data is discussed in the SI.

The a-SEI over the L^{3}ME electrodes has a sharp composition (PEO and $LiNO_3$) like that observed by XPS (see Fig. 2). After cycling L^{3}ME electrodes show bands in the N-O and C-O stretching regions likely assigned to the remaining aSEI as well as the vibrational fingerprints of Li_2CO_3 and Li_2O are observed. This spectroscopic evidence couples and extends the SEM evidence shown in the Fig. 4, where the resilience of the LIPSS morphology after cycling has been proved. Overall, FTIR and SEM prove the resilience of both ripples' morphology and aSEI composition.

On passing one may report that the SEI layer deposited over copper is highly amorphous and dominated by a strong band at 400–700 cm^{-1}, likely due to lithium oxides, and broad bands in the polyether C-O stretching regions. This SEI composition however promotes the growth of lithium dendrites as clearly demonstrated in the Fig. 4e.-f and by EIS is the figure S11a in the SI.

The strong promotion of the electrochemical deposition/dissolution of lithium and its reversibility on L^{3}ME compared to standard Cu electrodes inevitably originates from the different electrode kinetics induced by the simultaneous effect of LIPSS mesostructures and aSEI. The analysis of the overvoltages at various current densities and the corresponding Butler-Volmer parameters are shown in the Fig. 6 (see the methodological section for the technical details of the experiment and the data analysis).

A summary of the Butler-Volmer fit parameters estimated for SS, Cu, Cu@C and L^{3}ME electrodes is reported in the SI table S4. Quantitatively electro-kinetic parameters are in line with the literature benchmarks measured on rotating disk electrodes and similar carbonate-based liquid electrolytes [79].

The exchange current (J_0) is three times larger for the L^{3}ME electrodes compared to the copper: this is direct evidence of a faster electrochemical reduction/oxidation of Li on L^{3}ME compared to Cu, as well as SS. Apparently only the very large surface area provided by the Cu@C electrode allows to outperform L^{3}ME in terms of exchange current density (See SI table S4).

On the other hand, the anodic charge transfer coefficient (β) estimated on L^{3}ME is 0.392 ± 0.097, thus suggesting a hindered electrochemical lithium dissolution kinetics. All the other substrates, i.e. Cu, SS and C@Cu, shows a β value above 0.5, that implies an easier lithium dissolution and an hindered lithium deposition. This difference in the electro-kinetics is remarkable as it parallels the very different reversibility upon repeated lithium deposition/dissolution cycles. Apparently, the combination of LIPSS patterning and aSEI coating boosts the plating/stripping reversibility through the hindering of lithium dissolution.

One may speculate that a slower stripping, compared to plating, limits the selective dissolution of lithium from the base of dendrites, whereas an easier deposition, compared to dissolution, promotes the nucleation of a larger number of lithium seeds, thus limiting the growth of big dendrites. Overall, the combination of LIPSS and aSEI allows to enhance the electro-kinetics by facilitating the lithium deposition at a larger extent than the dissolution.

To highlight the synergistic cooperation of LIPSS and aSEI, we tested uncoated LIPSS@SS and bare SS disks coated with the aSEI (namely SS@E coated with a-SEI9@Li, see the SI application note 2). Here our aim is to decouple the individual effect of LIPSS and aSEI in galvanostatic tests to evaluate the lithium plating/stripping reversibility and to derive the electro-kinetic parameters. The comparison of the CEs measured at room temperature are shown in the SI figure S12 (SI) for SS@E and LIPSS@SS electrodes whereas Butler-Volmer fit parameters estimated for the same electrodes are reported in the SI table S5.

The CEs of both LIPSS@SS and SS@E electrodes outperform the SS bare disks achieving very good reversibility with few cycles with CE< 100 %. As expected, both materials underperform the outstanding performance of L^{3}ME. It is to be noted that upon cycling both SS@E and LIPSS@SS performance deteriorates with a decrease of CE and an increase of scattering performance. These features are electrochemical evidence of the accumulation of dead lithium over the surface of SS, SS@E and LIPSS@SS electrodes, whereas L^{3}ME ones strongly limits this drawback (see above and in particular the Fig. 4). Direct experimental evidence of the accumulation of degradation by-products and dead lithium is shown in the SI, figure S13, for SS, SS@E and LIPSS@SS *postmortem* electrodes after cycling.

Turning to the electro-kinetics derived from the Butler-Volmer fitting, both SS@E and LIPSS@SS materials shows 2- and 3.5-times larger exchange currents compared to the bare SS and the β values are in both cases smaller than 0.5. In this view, LIPSS patterning and aSEI coatings improves independently the kinetics of stripping/deposition, particularly in favor of the electrochemical nucleation/growth of lithium metal. It is a matter of fact that LIPSS and aSEI combination reinforces their individual beneficial effects on the stripping/deposition electrochemical process, being the exchange current of the L^{3}ME electrode 7 times larger compared to the bare SS. It is interesting to note that the L^{3}ME β value (i.e. 0.392 ± 0.097) closely matches that measured for LIPSS@SS electrodes (i.e. 0.415 ± 0.126), thus suggesting a specific role of the LIPSS-modified surface to hamper the electrochemical dissolution

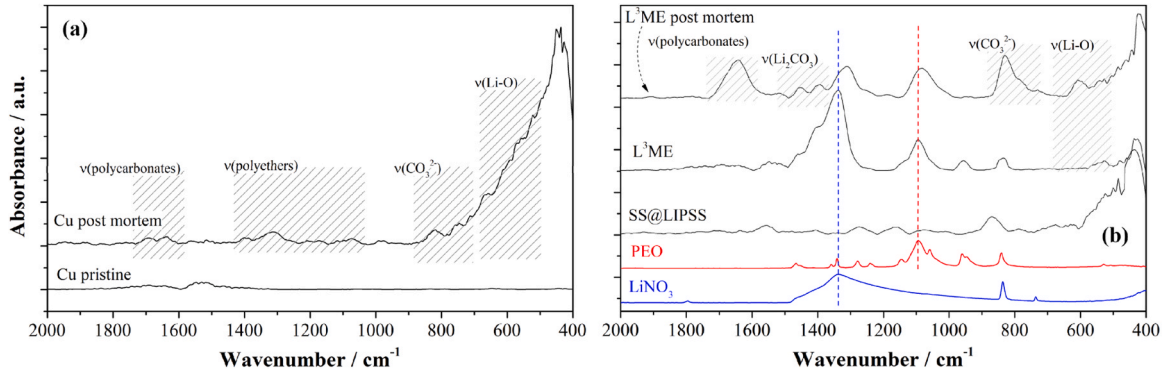

Fig. 5. FTIR spectra of the (a) Cu and (b) L^{3}ME electrodes collected *post mortem* from a lithium cell after 200 cycles of plating/stripping (Q_{lim} = 0.25 mAhcm^{-2} at J = 0.25 mAcm^{-2}).

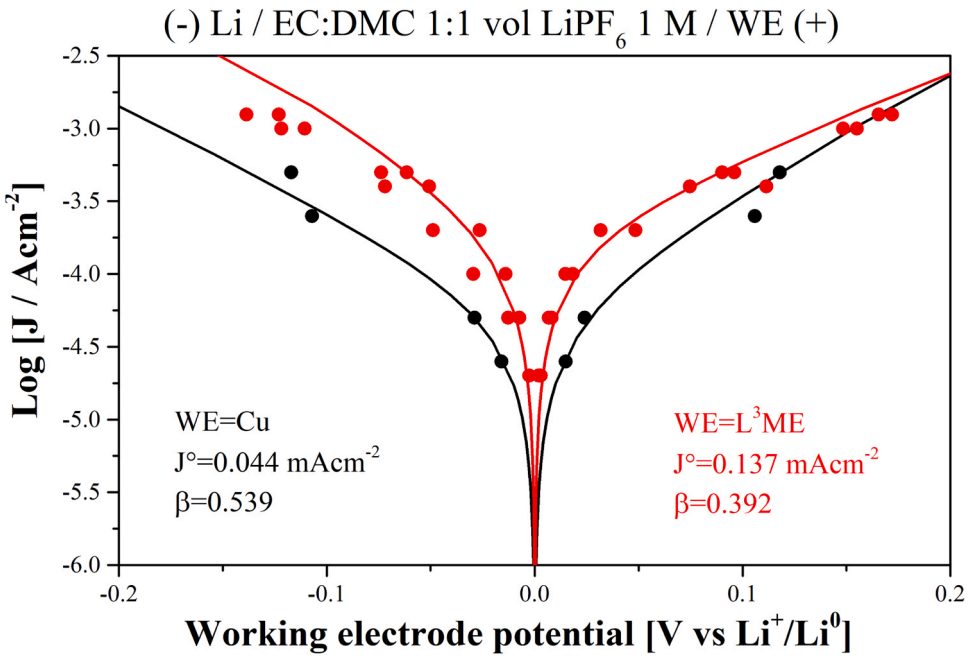

Fig. 6. Comparative analysis of the overpotentials measured at various current densities at room temperature upon plating/stripping lithium to/from Cu disks or L^3ME electrodes.

of lithium.

The formation of Laser-Induced Periodic Surface Structures (LIPSS) is governed by several factors related to laser parameters and the material properties of the substrate. Specifically, the characteristics of laser irradiation, such as pulse duration, scanning speed, and interline distance, significantly influence the resulting surface morphology. Studies indicate that these conditions must be finely tuned to achieve distinct nano-architectures on the target surface. Having demonstrated that the ability of L^3ME electrodes to deliver highly reversible lithium metal plating and stripping and discussed the origin of this behavior, as a final point it is interesting to analyze the impact of the LIPSS manufacture morphology on the electrochemical performance in lithium cells. In the application note 5 of the SI, we discuss the analysis of the morphology of different LIPSS substrates by using numerical image analysis algorithms able to discriminate the regularity (periodicity, variability, and linearity) of the LIPSS patterns. Three different substrates, namely LIPSS@SS, LIPSS@SS' and LIPSS@SS'' have been manufactured by applying different manufacturing conditions: these materials show qualitatively a trend in the ripples' regularity distribution LIPSS@SS>LIPSS@SS'>LIPSS@SS'' (see figures S14, S15 and tables S6, S7 in the SI). The performance in lithium cell of the three L^3ME composite electrodes, manufactured starting from the three different LIPSS substrates each coated with the same aSEI, demonstrates that only LIPSS@SS one is able to sustain a reversible Li plating/stripping in a variety of galvanostatic conditions, whereas both others fails to different extent (see the figure S16 in the SI). Thus, the reversibility of the plating/stripping deposition of lithium onto these L^3ME electrodes is remarkably driven by the regularity (periodicity, variability and linearity) of the underneath morphology of the LIPSS substrate. Further studies are necessary to elucidate in detail the interplay between LIPSS manufacturing and performance, but this scope is beyond the goal of this work that proved for the first time in the literature the idea of the combined and synergistic use of LIPSS and aSEI to promote the reversible plating/stripping of lithium in aprotic electrolytes. However some general considerations and speculations are appropriate based on the results and the state-of-the-art understanding of metallic lithium plating/stripping electrochemical reactions.

Overall, the observed effects of various laser-induced periodic surface structures (LIPSS) patterning conditions and the compositions of artificial Solid Electrolyte Interphase (aSEI) on electrochemical performance are likely linked to modifications of mass transport behavior, electrochemical reaction kinetics, interfacial stability, and Li+ ion diffusion. In fact, different LIPSS patterning conditions can influence surface morphology, which can significantly affect mass transport behavior. Specific surface patterns can enhance the surface area available for lithium nucleation and plating, optimizing the diffusion pathway for Li^+ ions. Well-defined nano-structures tend to promote more homogeneous lithium deposition, thereby reducing the likelihood of dendrite formation, which poses a significant challenge for traditional lithium battery architectures. The electrochemical reaction kinetics are also substantially impacted by LIPSS patterns. Enhanced electrode kinetics are observed due to higher exchange current density resulting from finer surface structures. These patterns can enable more efficient electrochemical reactions by minimizing concentration polarization and allowing for faster ion transport to the interface. Additionally, electrochemical kinetics are influenced by the composition and formation of the aSEI layer, which can stabilize the interface and provide favorable ionic conductivity while preventing unwanted side reactions. The improved interfacial stability is another critical factor that affects performance and likely contributes to the functional properties of L^3ME electrodes. The nature of the aSEI formed on LIPSS-patterned surfaces can vary significantly based on the surface characteristics and the electrolyte employed. A well-optimized aSEI layer enhances interfacial stability, facilitating smoother lithium plating and stripping while minimizing impedance related to lithium-ion transport. Furthermore, tuning electrolyte formulations can enhance passivation layer formation, leading to improved electro-crystallization and dissolution behavior.

Conclusion

The combined use of LIPSS and aSEI coating allows a tailored modification of the surface of SS thin disks. The modified SS-based foils, namely L^3ME, are mechanically solid, completely lithium-less and can handled in dry air without the need of Ar confinement. This approach goes well beyond the standard strategies to manufacture anodeless

electrodes.

The functional properties of L^3ME disks have been demonstrated in electrochemical lithium metal cells using Celgard separators soaked with a $LiPF_6$ EC:DMC aprotic electrolyte. L^3ME electrodes are able to host reversible electrochemical metallic lithium deposition/stripping at constant current density for hundred of cycles at room temperature. Negligible accumulation of dead lithium is observed after cycling, whereas the LIPSS mesostructured patterns are preserved. The improved performance of L^3ME in lithium cells originates from the synergic beneficial effects of LIPSS and aSEI coating. Both strategies improve the electro-kinetics of the stripping/deposition, in particular in favor of the lithium nucleation/growth.

The use of LIPSS to draw regular mesostructured patterns over the surface of anode-less metal electrodes is here demonstrated for the first time in the literature, as well as its combination with the deposition of a tailored artificial solid electrolyte interphase before cell assembly. Both strategies can be easily modified to target specific morphologies and surface moieties, as an example by changing the aSEI composition (polymer binder, inorganic additives and ratio), the metal substrate for LIPSS (e.g. SS, copper, aluminum, titanium,….) and the LIPSS conditions (laser fluence, incidence direction and wavelength, sample scanning speed, interline distance, number of accumulated laser pulses, …). This synergic approach has a very limited environmental fingerprint, and it is easily scalable, as it barely implies the use of solvents whereas it avoids high temperature treatments or expensive chemical products, as well as it can be easily exported to industrial conditions, as the treatments are performed under ambient conditions.

Overall, this study is the first step in a totally unexplored direction to develop a simple, effective and extremely flexible strategy for the manufacture of lithium less Li metal electrodes able to reversibly support the deposition/stripping of lithium metal in electrochemical cells. Further enhancing battery performance can be approached through several promising directions. Tuning the electrolyte formulation is critical; optimizing the composition can facilitate effective passivation film formation on lithium, subsequently enhancing electrochemical stability and efficiency. Focused research into hybrid electrolyte systems that combine the benefits of liquid and solid-state technologies also presents a valuable avenue for performance improvement. Additionally, continuous advancements in patterning techniques to refine the LIPSS structures could yield further enhancements in lithium deposition uniformity and overall electrochemical kinetics.

CRediT authorship contribution statement

Maria Assunta Navarra: Writing – review & editing, Supervision, Resources. **Nicholas Carboni:** Visualization, Validation, Methodology, Investigation, Formal analysis, Data curation. **Claudio Gerbaldi:** Writing – review & editing, Writing – original draft, Supervision. **Roberto Teghil:** Writing – review & editing, Methodology. **Gabriele Lingua:** Writing – review & editing, Resources. **Angela De Bonis:** Writing – review & editing, Methodology, Investigation. **Marisa Falco:** Writing – review & editing, Resources. **Mariangela Curcio:** Investigation. **Giuseppe Antonio Elia:** Writing – review & editing. **Daniele Maria Trucchi:** Investigation. **Paola Gislon:** Writing – review & editing, Project administration, Funding acquisition. **Maria Lucia Pace:** Writing – review & editing, Investigation. **Laura Silvestri:** Writing – review & editing, Methodology. **Antonio Santagata:** Writing – review & editing, Methodology, Investigation. **Andrea Ceppetelli:** Writing – review & editing, Writing – original draft, Visualization, Validation, Methodology, Investigation, Formal analysis, Data curation. **Sergio Brutti:** Writing – review & editing, Writing – original draft, Visualization, Resources, Project administration, Methodology, Investigation, Funding acquisition, Data curation, Conceptualization. **Luca Mesina:** Investigation. **Arianna Sette:** Investigation. **Marco Agostini:** Writing – review & editing, Methodology, Investigation. **Andrea Gentile:** Investigation, Formal analysis, Data curation.

Declaration of Competing Interest

The authors declare the following financial interests/personal relationships which may be considered as potential competing interests: Sergio Brutti reports financial support, administrative support, and equipment, drugs, or supplies were provided by University of Rome La Sapienza. If there are other authors, they declare that they have no known competing financial interests or personal relationships that could have appeared to influence the work reported in this paper.

Acknowledgements

This research was funded by Italian Ministry of Economic Development through ENEA in the frame of the “Ricerca Sistema Elettrico” PTR program 2025–2027. This study was carried out within the NEST—Network for Energy Sustainable Transition and received funding from the European Union Next-Generation EU (PIANO NAZIONALE DI RIPRESA E RESILIENZA (PNRR)—MISSIONE 4 COMPONENTE 2, INVESTIMENTO 1.3—D.D. 1561 11/10/2022, B53C22004070006). This manuscript reflects only the authors’ views and opinions, neither the European Union nor the European Commission can be considered responsible for them. All Sapienza staff within the NEST project participate to this action under the frame of the grant PE2421852F05911E. This study was carried out also within the MOST−Sustainable Mobility Center and received funding from the European Union Next-GenerationEU (PIANO NAZIONALE DI RIPRESA E RESILIENZA−PNRR e MISSIONE 4 COMPONENTE 2, INVESTIMENTO 1.4 e D.D. 1033 June 17, 2022, CN00000023, Spoke 13). This manuscript reflects only the authors’ views and opinions, and neither the European Union nor the European Commission can be considered responsible for them. C.G., G.A.E. and M.F acknowledge support under the MUR program ′Dipartimenti di Eccellenza 2023–2027″ (CUPE17G22001490006). A.S. and M.L.P. acknowledge the Project funded by the European Union - NextGenerationEU under the National Recovery and Resilience Plan project IR0000027, CUP: B33C22000710006 - iENTRANCE@ENL: Infrastructure for Energy TRAnsition aNd Circular Economy @ EuroNanoLab.

Appendix A. Supporting information

Supplementary data associated with this article can be found in the online version at doi:10.1016/j.fub.2025.100095.

Data availability

Data will be made available on request.

References

[1] J. Piątek, S. Afyon, T.M. Budnyak, S. Budnyk, M.H. Sipponen, A. Slabon, Sustainable Li-ion batteries: chemistry and recycling, Adv. Energy Mater. 11 (2021) 2003456, https://doi.org/10.1002/aenm.202003456.
[2] S.-Y. Yang, V. Sencadas, S.S. You, N.Z.-X. Jia, S.S. Srinivasan, H.-W. Huang, A. E. Ahmed, J.Y. Liang, G. Traverso, Powering implantable and ingestible electronics, Adv. Funct. Mater. 31 (2021) 2009289, https://doi.org/10.1002/adfm.202009289.
[3] S. Ferrari, M. Falco, A.B. Muñoz-García, M. Bonomo, S. Brutti, M. Pavone, C. Gerbaldi, Solid-state post Li metal ion batteries: a sustainable forthcoming reality? Adv. Energy Mater. 11 (2021) 2100785 https://doi.org/10.1002/aenm.202100785.
[4] M. Parrilla, K. de Wael, Wearable self-powered electrochemical devices for continuous health management, Adv. Funct. Mater. 31 (2021) 210742, https://doi.org/10.1002/adfm.202107042.
[5] C. Zhang, K. Huang, A comprehensive review on the development of solid-state metal–air batteries operated on oxide-ion chemistry, Adv. Energy Mater. 11 (2021) 2000630, https://doi.org/10.1002/aenm.202000630.
[6] V. Vallem, Y. Sargolzaeiaval, M. Ozturk, Y.-C. Lai, M.D. Dickey, Energy harvesting and storage with soft and stretchable materials, Adv. Mater. 33 (2021) 2004832, https://doi.org/10.1002/adma.202004832.

[7] Y. Chen, T. Wang, H. Tian, D. Su, Q. Zhang, G. Wang, Advances in lithium–sulfur batteries: from academic research to commercial viability, Adv. Mater. 33 (2021) 2003666, https://doi.org/10.1002/adma.202003666.

[8] W. Zhang, H. Liu, X. Zhang, X. Li, G. Zhang, P. Cao, 3D printed micro-electrochemical energy storage devices: from design to integration, Adv. Funct. Mater. 31 (2021) 2104909, https://doi.org/10.1002/adfm.202104909.

[9] T. Xu, H. Du, H. Liu, W. Liu, X. Zhang, C. Si, P. Liu, K. Zhang, Advanced nanocellulose-based composites for flexible functional energy storage devices, Adv. Mater. 33 (2021) 2101368, https://doi.org/10.1002/adma.202101368.

[10] F. Duffner, N. Kronemeyer, J. Tübke, J. Leker, M. Winter, R. Schmuch, Post-lithium-ion battery cell production and its compatibility with lithium-ion cell production infrastructure, Nat. Energy 6 (2021) 123, https://doi.org/10.1038/s41560-020-00748-8.

[11] Y. Tian, G. Zeng, A. Rutt, T. Shi, H. Kim, J. Wang, J. Koettgen, Y. Sun, B. Ouyang, T. Chen, Z. Lun, Z. Rong, K. Persson, G. Ceder, Promises and challenges of next-generation "beyond li-ion" batteries for electric vehicles and grid decarbonization, Chem. Rev. 121 (2021) 1623 (Promises and Challenges of Next-Generation "beyond Li-ion" Batteries for Electric Vehicles and Grid Decarbonization).

[12] B. Scrosati, J. Garche, Lithium batteries: status, prospects and future, J. Power Sources 195 (2010) 2419, https://doi.org/10.1016/j.jpowsour.2009.11.048.

[13] B. Scrosati, Technology: charging towards the superbattery, Nature 473 (2011) 448, https://doi.org/10.1038/473448a.

[14] J. Hassoun, B. Scrosati, Review—advances in anode and electrolyte materials for the progress of lithium-ion and beyond lithium-ion batteries, J. Electrochem. Soc. 162 (2015) A2582, https://doi.org/10.1149/2.0191514jes.

[15] P.G. Bruce, B. Scrosati, J.-M. Tarascon, Nanomaterials for rechargeable lithium batteries, Angew. Chem. Int. Ed. 47 (2008) 2930, https://doi.org/10.1002/anie.200702505.

[16] K. Turcheniuk, D. Bondarev, G.G. Amatucci, G. Yushin, Battery materials for low-cost electric transportation, Mater. Today 42 (2021) 57, https://doi.org/10.1016/j.mattod.2020.09.027.

[17] H. Zhang, Y. Yang, D. Ren, L. Wang, X. He, Graphite as anode materials: fundamental mechanism, recent progress and advances, Energy Storage Mater. 36 (2021) 147, https://doi.org/10.1016/j.ensm.2020.12.027.

[18] L. Xie, C. Tang, Z. Bi, M. Song, Y. Fan, C. Yan, X. Li, F. Su, Q. Zhang, C. Chen, Adv. Energy Mater. 11 (2021), https://doi.org/10.1002/aenm.202101650.

[19] H. Kim, K.R. Pyun, M.-T. Lee, H.B. Lee, S.H. Ko, Recent advances in sustainable wearable energy devices with nanoscale materials and macroscale structures, Adv. Funct. Mater. (2021), https://doi.org/10.1002/adfm.202110535.

[20] M. Steen, N. Lebedeva, F.Di Persio, L. Brett, EU Competitiveness in Advanced Li-ion Batteries for E-Mobility and Stationary Storage Applications – Opportunities and Actions, EUR 28837 EN, Publications Office of the European Union, Luxembourg, 2017, https://doi.org/10.2760/75757.

[21] Md Adil, A. Sarkar, A. Roy, M.R. Panda, A. Nagendra, S. Mitra, Practical aqueous calcium-ion battery full-cells for future stationary storage, ACS Appl. Mater. Interfaces 12 (2020) 11489, https://doi.org/10.1021/acsami.9b20129.

[22] X. Ji, A paradigm of storage batteries, Energy Environ. Sci. 12 (2019) 3203, https://doi.org/10.1039/C9EE02356A.

[23] D. Larcher, J.-M. Tarascon, Towards greener and more sustainable batteries for electrical energy storage, Nat. Chem. 7 (2014) 19, https://doi.org/10.1038/nchem.2085.

[24] M.T. McDowell, S.W. Lee, W.D. Nix, Y. Cui, 25th Anniversary article: understanding the lithiation of silicon and other alloying anodes for lithium-ion batteries, Adv. Mater. 25 (2013) 4966–4985, https://doi.org/10.1002/adma.201301795.

[25] A.-L. Dalverny, J.-S. Filhol, M.-L. Doublet, Interface electrochemistry in conversion materials for Li-ion batteries, J. Mater. Chem. 21 (2011) 10134–10142, https://doi.org/10.1039/C0JM04202A.

[26] S.H. Yu, S.H. Lee, D.J. Lee, Y.E. Sung, T. Hyeon, Conversion reaction-based oxide nanomaterials for lithium ion battery anodes, Small 12 (2016) 2146–2172, https://doi.org/10.1002/smll.201502299.

[27] C. Wu, S.-X. Dou, Y. Yu, The state and challenges of anode materials based on conversion reactions for sodium storage, Small 14 (2018) 1703671, https://doi.org/10.1002/smll.201703671.

[28] N. Mahne, O. Fontaine, M. Ottakam Thotiyl, M. Wilkening, S. Freunberger, Mechanism and performance of lithium-oxygen batteries – a perspective, Chem. Sci. 8 (2017) 6716–6729, https://doi.org/10.1039/C7SC02519J.

[29] P.G. Bruce, S. Freunberger, L.J. Hardwick, J.-M. Tarascon, Li-O_2 and Li-S batteries with high energy storage, Nat. Mater. 11 (2012) 19–29, https://doi.org/10.1038/nmat3191.

[30] L. Grande, E. Paillard, J. Hassoun, J.-B. Park, Y.-J. Lee, Y.-K. Sun, S. Passerini, B. Scrosati, The lithium/air battery: still an emerging system or a practical reality? Adv. Mater. 27 (2015) 784–800, https://doi.org/10.1002/adma.201403064.

[31] M.J. Lacey, A. Yalamanchili, J. Maibach, C. Tengstedt, K. Edström, D. Brandell, The Li-S battery: an investigation of redox shuttle and self-discharge behaviour with LiNO3-containing electrolytes, RSC Adv. 6 (2016) 3632–3641, https://doi.org/10.1039/c5ra23635e.

[32] M.E. Arroyo-De Dompablo, A. Ponrouch, P. Johansson, M.R. Palacín, K. v Nielson, T.L. Liu, A. Ponrouch, J. Bitenc, R. Dominko, N. Lindahl, P. Johansson, M. R. Palacin, Multivalent rechargeable batteries, Energy Storage Mater. 20 (2019) 253–262, https://doi.org/10.1016/j.ensm.2019.04.012.

[33] M. Li, J. Lu, X. Ji, Y. Li, Y. Shao, Z. Chen, C. Zhong, K. Amine, Design strategies for nonaqueous multivalent-ion and monovalent-ion battery anodes, Nat. Rev. Mater. 5 (2020) 276–294, https://doi.org/10.1038/s41578-019-0166-4.

[34] A. Ponrouch, C. Frontera, F. Bardé, M.R. Palacín, Towards a calcium-based rechargeable battery, Nat. Mater. 15 (2016) 169–172, https://doi.org/10.1038/nmat4462.

[35] J. Wen, Y. Yu, C. Chen, A review on lithium-ion batteries safety issues: existing problems and possible solutions, Mater. Express 2 (2012) 197–212, https://doi.org/10.1166/mex.2012.1075.

[36] P.A. Nelson, S. Ahmed, K.G. Gallagher, D.W. Dees. Modeling the Performance and Cost of Lithium-Ion Batteries for Electric-Drive Vehicles, third ed, Argonne, IL (United States), 2019.

[37] K. Qin, K. Holguin, M. Mohammadiroudbari, J. Huang, E.Y.S. Kim, R. Hall, C. Luo, Strategies in structure and electrolyte design for high-performance lithium metal batteries, Adv. Funct. Mater. 31 (2021) 2009694, https://doi.org/10.1002/adfm.202009694.

[38] J.H. Um, S.-H. Yu, Unraveling the mechanisms of lithium metal plating/stripping via in situ/operando analytical techniques, Adv. Energy Mater. 11 (2021) 2003004, https://doi.org/10.1002/aenm.202003004.

[39] X. Wang, W. Mai, X. Guan, Q. Liu, W. Tu, W. Li, F. Kang, B. Li, Recent advances of electroplating additives enabling lithium metal anodes to applicable battery techniques, Energy Environ. Mater. 4 (2021) 284–292, https://doi.org/10.1002/eem2.12109.

[40] C. Jiang, C. Ma, F. Yang, X. Cai, Y. Liu, X. Tao, Materials chemistry among the artificial solid electrolyte interphases of metallic lithium anodes, Mater. Chem. Front. 5 (2021) 5194–5210, https://doi.org/10.1039/d1qm00352f.

[41] G.M. Hobold, J. Lopez, R. Guo, N. Minafra, A. Banerjee, Y. Shirley Meng, Y. Shao-Horn, B.M. Gallant, Moving beyond 99.9% Coulombic efficiency for lithium anodes in liquid electrolytes, Nat. Energy 6 (2021) 951–960, https://doi.org/10.1038/s41560-021-00910-w.

[42] C. Heubner, S. Maletti, H. Auer, J. Hüttl, K. Voigt, O. Lohrberg, K. Nikolowski, M. Partsch, A. Michaelis, From lithium-metal toward anode-free solid-state batteries: current developments, issues, and challenges, Adv. Funct. Mater. 31 (2021) 2106608, https://doi.org/10.1002/adfm.202106608.

[43] Y. Xiang, M. Tao, G. Zhong, Z. Liang, G. Zheng, X. Huang, X. Liu, Y. Jin, N. Xu, M. Armand, R. Fu, Y. Yang, Quantitatively analyzing the failure processes of rechargeable Li metal batteries, Sci. Adv. 7 (2021) eabj3423, https://doi.org/10.1126/sciadv.abj3423.

[44] B. Horstmann, J. Shi, R. Amine, M. Werres, X. He, H. Jia, F. Hausen, I. Cekic-Laskovic, S. Wiemers-Meyer, J. Lopez, R. Kostecki, A. Latz, Strategies towards enabling lithium metal in batteries: interphases and electrodes, Energy Environ. Sci. 14 (2021) 5289–5314, https://doi.org/10.1039/d1ee00767j.

[45] E. Peled, D. Golodnitsky, G. Ardel, Advanced model for solid electrolyte interphase electrodes in liquid and polymer electrolytes, J. Electrochem. Soc. 144 (1997) L208, https://doi.org/10.1149/1.1837858.

[46] M. Montanino, S. Passerini, G.B. Appetecchi, Electrolytes for rechargeable lithium batteries. Rechargeable Lithium Batteries: From Fundamentals to Applications, Elsevier Inc, 2015, pp. 73–116, https://doi.org/10.1016/B978-1-78242-090-3.00004-3.

[47] T. Kawamura, S. Okada, J. Yamaki, Decomposition reaction of LiPF6-based electrolytes for lithium ion cells, J. Power Sources 156 (2006) 547–554, https://doi.org/10.1016/j.jpowsour.2005.05.084.

[48] P. Johansson, P. Jacobsson, Rational design of electrolyte components by ab initio calculations, in: Journal of Power Sources, 153, Elsevier, 2006, pp. 336–344, https://doi.org/10.1016/j.jpowsour.2005.05.048.

[49] M.D. Tikekar, S. Choudhury, Z. Tu, L.A. Archer, Design principles for electrolytes and interfaces for stable lithium-metal batteries, Nat. Energy 1 (2016) 16114, https://doi.org/10.1038/nenergy.2016.114.

[50] S.A. Han, H. Qutaish, M.-S. Park, J. Moon, J.H. Kim, Strategic approaches to the dendritic growth and interfacial reaction of lithium metal anode, Chem. Asian J. 16 (2021) 4010–4017, https://doi.org/10.1002/asia.202101108.

[51] S. Fang, Y. Zhang, X. Liu, Lithium anode in carbonate-based electrolyte: high-performance by self-protected solid-electrolyte-interphase, Chem. Eng. J. 426 (2021) 131880, https://doi.org/10.1016/j.cej.2021.131880.

[52] P. Shi, Z.-Y. Liu, X.-Q. Zhang, X. Chen, N. Yao, J. Xie, C.-B. Jin, Y.-X. Zhan, G. Ye, J.-Q. Huang, T. Maria-Magdalena, Q. Zhang, Polar interaction of polymer host–solvent enables stable solid electrolyte interphase in composite lithium metal anodes, J. Energy Chem. 64 (2022) 172–178, https://doi.org/10.1016/j.jechem.2021.04.045.

[53] S. Kim, S.O. Park, M.-Y. Lee, J.-A. Lee, I. Kristanto, T.K. Lee, D. Hwang, J. Kim, T.-U. Wi, H.-W. Lee, S.K. Kwak, N.-S. Choi, Stable electrode–electrolyte interfaces constructed by fluorine- and nitrogen-donating ionic additives for high-performance lithium metal batteries, Energy Storage Mater. 45 (2022) 1–13, https://doi.org/10.1016/j.ensm.2021.10.031.

[54] L. Fan, B. Sun, K. Yan, P. Xiong, X. Guo, Z. Guo, N. Zhang, Y. Feng, K. Sun, G. Wang, A dual-protective artificial interface for stable lithium metal anodes, Adv. Energy Mater. 11 (2021) 2102242, https://doi.org/10.1002/aenm.202102242.

[55] G. Li, H. Li, Y. Wang, D. Xiong, S. Wang, Y. Yan, S. Chen, B. Tian, Y. Shi, Suppressing li dendrite puncture with a hierarchical h-BN protective layer, ACS Appl. Mater. Interfaces 13 (2021) 56109–56115, https://doi.org/10.1021/acsami.1c15980.

[56] X. Liu, P. Xu, J. Zhang, X. Hu, Q. Hou, X. Lin, M. Zheng, Q. Dong, A highly reversible lithium metal anode by constructing lithiophilic Bi-nanosheets, Small 17 (2021) 2102016, https://doi.org/10.1002/smll.202102016.

[57] C. Chen, Q. Liang, Z. Chen, W. Zhu, Z. Wang, Y. Li, X. Wu, X. Xiong, Phenoxy Radical-Induced Formation of Dual-Layered Protection Film for High-Rate and Dendrite-Free Lithium-Metal *Angewandte*, Chem. Int. Ed. 60 (2021) 26718–26724, https://doi.org/10.1002/anie.202110441.

[58] T.-T. Su, J.-B. Le, W.-F. Ren, S.-J. Zhang, J.-M. Yuan, K. Wang, C.-Y. Shao, J.-T. Li, S.-G. Sun, R.-C. Sun, Heteroatom-rich polymers as a protective film to control lithium growth for high-performance lithium-metal batteries, J. Power Sources 521 (2022) 230949, https://doi.org/10.1016/j.jpowsour.2021.230949.
[59] G. He, Q. Li, Y. Shen, Y. Ding, Flexible Amalgam Film Enables Stable Lithium Metal Anodes with High Capacities, Angew. Chem. Int. Ed. 58 (2019) 18466, https://doi.org/10.1002/anie.201911800.
[60] J. Lou, G. Wang, Y. Xia, C. Liang, H. Huang, Y. Gan, X. Tao, J. Zhang, W. Zhang, Achieving efficient and stable interface between metallic lithium and garnet-type solid electrolyte through a thin indium tin oxide interlayer, J. Power Sources 448 (2020) 227440, https://doi.org/10.1016/j.jpowsour.2019.227440.
[61] Z. Zeng, S. Wang, J. Cheng, G. Hou, D. Li, G. Han, L. Ci. Spontaneous in Situ Surface Alloying of Li-Zn Derived from a Novel Zn2 >-Containing Solid Polymer Electrolyte for Steady Cycling of Li Metal Battery ACS Sustainable Chemistry and Engineering 2021, 9, 4282 DOI 10.1021/acssuschemeng.1c00878.
[62] L. He, Q. Sun, L. Lu, S. Adams, Understanding and Preventing Dendrite Growth in Lithium Metal Batteries, ACS Appl. Mater. Interfaces 13 (2021) 34320–34331, https://doi.org/10.1021/acsami.1c08268.
[63] X.-R. Chen, X. Chen, C. Yan, X.-Q. Zhang, Q. Zhang, J.-Q. Huang, Role of Lithiophilic Metal Sites in Lithium Metal Anodes, Energy Fuels 35 (2021) 12746–12752, https://doi.org/10.1021/acs.energyfuels.1c01602.
[64] X. He, F. Yan, M. Gao, Y. Shi, G. Ge, B. Shen, J. Zhai, Cu-Doped Alloy Layer Guiding Uniform Li Deposition on a Li-LLZO Interface under High Current, ACS Appl. Mater. Interfaces 13 (2021) 42212–42219, https://doi.org/10.1021/acsami.1c11607.
[65] Z.L. Zhang, Y. Jin, Y. Zhao, J. Xu, B. Sun, K. Liu, H. Lu, N. Lv, Z. Dang, H. Wu, Homogenous lithium plating/stripping regulation by a mass-producible Zn particles modified Li-metal composite anode, Nano Res. 14 (2021) 3999–4005, https://doi.org/10.1007/s12274-021-3326-y.
[66] H. Song, T. He, J. Liu, Y. Wang, X.L. Li, J. Liu, D. Zhang, H.Y. Yang, J. Hu, S. Huang, Conformal coating of lithium-zinc alloy on 3D conducting scaffold for high areal capacity dendrite-free lithium metal batteries, Carbon 181 (2021) 99–106, https://doi.org/10.1016/j.carbon.2021.05.002.
[67] C. Wang, M. Liu, M. Thijs, F.G.B. Ooms, S. Ganapathy, M. Wagemaker, High dielectric barium titanate porous scaffold for efficient Li metal cycling in anode-free cells, Nat. Commun. 12 (2021) 6536, https://doi.org/10.1038/s41467-021-26859-8.
[68] Y. Xie, Z. Han, H. Li, J. Hu, L. Zhang, A. Wang, S. Chang, J. Xu, C. Liu, Y. Lai, Y. Lai, Z. Zhang, Uniform nucleation of sodium/lithium in holey carbon nanosheet for stable Na/Li metal anodes, Chem. Eng. J. 427 (2022) 130959, https://doi.org/10.1016/j.cej.2021.130959.
[69] J. Walton, Peak Fitting with CasaXPS: A Casa Pocket Book, ISBN 978-0954953317, Acolyte Science, Knutsford, UK, 2010.
[70] M.D. Abràmoff, P.J. Magalhães, S.J. Ram, Image processing with imageJ, Biophotonics Int. 11 (2004) 36–41. ISSN 10818693.
[71] S. Gräf, F.A. Müller, Polarisation-dependent generation of fs-laser induced periodic surface structures, Appl. Surf. Sci. 331 (2015) 150–155, https://doi.org/10.1016/j.apsusc.2015.01.056.
[72] L. Chen, Z. Chen, K. Shimada, M. Mizutani, T. Kuriyagawa, Laser–induced nanopillar structures around particles, Appl. Surf. Sci. 572 (2022) 151453, https://doi.org/10.1016/j.apsusc.2021.151453.
[73] E. Maggiore, I. Mirza, D. Dellasega, M. Tommasini, P.M. Ossi, Sliding on snow of Aisi 301 stainless steel surfaces treated with ultra-short laser pulses, Appl. Surf. Sci. Adv. 7 (2022), https://doi.org/10.1016/j.apsadv.2021.100194.
[74] Z. Li, Q. Wu, X. Jiang, X. Zhou, Y. Liu, X. Hu, J. Zhang, J. Yao, J. Xu, Appl. Surf. Sci. 580 (2022) 100194, https://doi.org/10.1016/j.apsusc.2021.152107.
[75] Q. Wang, B. Liu, Y. Shen, J. Wu, Z. Zhao, C. Zhong, W. Hu, Confronting the challenges in lithium anodes for lithium metal batteries, Adv. Sci. 8 (2021) 2101111, https://doi.org/10.1002/advs.202101111.
[76] N.R. Geise, R.M. Kasse, J. Nelson Weker, H.-G. Steinrück, M.F. Toney, Quantification of efficiency in lithium metal negative electrodes via operando X-ray diffraction, Chem. Mater. 33 (2021) 7537–7545, https://doi.org/10.1021/acs.chemmater.1c02585.
[77] X.-R. Chen, C. Yan, J.-F. Ding, H.-J. Peng, Q. Zhang, New insights into “dead lithium” during stripping in lithium metal batteries, J. Energy Chem. 62 (2021) 289–294, https://doi.org/10.1016/j.jechem.2021.03.048.
[78] D. Aurbach, A. Zaban, Impedance spectroscope of lithium electrodes: Part 2. The behaviour in propylene carbonate solutions — the significance of the data, J. Electroanal. Chem. 367 (1994) 15–25, https://doi.org/10.1016/0022-0728(93)02998-W.
[79] X.-M. Wang, T. Nishina, I. Uchida, Application of the microelectrode technique to the kinetic study of lithium deposition/dissolution and alloying in organic solutions, J. Power Sources 68 (1997) 483–486, https://doi.org/10.1016/S0378-7753(97)02522-6.